

# Comparison of toroidicity-induced Alfvén eigenmodes and energetic particle modes by gyrokinetic particle simulations

Chenxi Zhang,<sup>1,2</sup> Wenlu Zhang,<sup>1,2,3,a)</sup> Zhihong Lin,<sup>3,4</sup> and Ding Li<sup>1,2</sup>

<sup>1</sup>Department of Modern Physics, University of Science and Technology of China, Hefei 230026, People's Republic of China

<sup>2</sup>Institute of Physics, Chinese Academy of Sciences, Beijing 100190, People's Republic of China

<sup>3</sup>Department of Physics and Astronomy, University of California, Irvine, California 92697, USA

<sup>4</sup>Fusion Simulation Center, Peking University, Beijing 100871, People's Republic of China

(Received 2 February 2013; accepted 15 April 2013; published online 2 May 2013)

This work reports on linear global gyrokinetic particle simulations of the excitation of toroidicity-induced Alfvén eigenmodes (TAE) and energetic particle modes (EPM), and the comparison between these two modes. The TAE excitation by antenna clarifies the magnetohydrodynamic (MHD) mode structure and the discrete eigenmode exists in the gap between the upper and lower accumulation points. The TAE excitation by fast ions modifies the MHD mode structure because of radial symmetry breaking and the eigenmode frequency moves towards the lower accumulation point. The phase space structure of fast ions shows that both passing and trapped particles contribute to the TAE excitation and that trapped particles dominate the wave-particle resonance in our simulations. The growth rate of TAE is sensitive to the fast ion energy, density, and density gradient, which are also important factors contributing to the transition of the TAE to the EPM. The gyrokinetic particle simulations also confirm the excitation of EPM when the drive is stronger. The frequency of the EPM is determined by the characteristic frequencies of fast ion motion in toroidal geometry. © 2013 AIP Publishing LLC. [<http://dx.doi.org/10.1063/1.4803502>]

## I. INTRODUCTION

Alfvén eigenmodes occurring in toroidal geometry, such as the toroidicity-induced Alfvén eigenmode (TAE), are significant phenomena that can cause fast ion loss in fusion devices. The interaction of Alfvén eigenmodes with fast ions is an important research topic concerning the development of future fusion devices such as the International Thermonuclear Experimental Reactor (ITER)<sup>1</sup> as fast ions can be produced through fusion reactions ( $\alpha$  particles), neutral beam injection (NBI), and radio frequency (RF) heating. The TAE is a gap mode and the gap is formed by two counterpropagating Alfvén waves with adjacent poloidal numbers,  $m$  and  $m+1$  for example, at the radial location when the two wave vectors have the same absolute values  $k_{||m} = -k_{||m+1}$ . The TAE mode is firstly predicted by magnetohydrodynamic (MHD) theory<sup>2,3</sup> in the radially local limit with two assumptions: First of all, the wavelengths of waves propagating perpendicular to the magnetic field are shorter than those waves propagating along the parallel direction. Further, the effects associated with the fast magnetosonic wave and the slow sound wave are ignored. The expression for TAE excitation by fast ions<sup>4</sup> is theoretically derived from the drift kinetic equation<sup>5</sup> of fast ions. In their later works,<sup>6,7</sup> Chen and his collaborators provide the fishbone-like dispersion relation of fast ion interaction with background plasmas, which can be used to estimate the stability of modes. The dispersion relation,  $-i\Lambda + \delta W_f + \delta W_k = 0$ , predicts the existence of two types of modes, the TAE and energetic particle modes (EPM). The difference between these two

modes is that TAE is an MHD gap mode whose frequency is determined by the background plasmas with  $\Re e \Lambda^2 < 0$ , while EPM is a mode in the continuum with its frequency corresponding to the characteristic frequency of fast ions with  $\Re e \Lambda^2 > 0$ . Zonca's theoretical works<sup>8-10</sup> demonstrate the details of the EPM structure. Subsequent to its theoretical prediction, the TAE was observed in the TFTR,<sup>11</sup> DIII-D,<sup>12</sup> JET,<sup>13</sup> JT-60U,<sup>14,15</sup> stellarators,<sup>16,17</sup> and other fusion reactors. There are several review papers on TAE regarding the physical process of the eigenmode. Ref. 18 provides a theoretical review of the interaction of the Alfvén eigenmodes with fast ions, and further a lengthy review regarding research in this field appeared in 1999.<sup>19</sup> Heidbrink's recent reviews<sup>20</sup> attend to the basic physics of the interaction of the Alfvén eigenmodes with fast ions and some experimental results also have been discussed therein. Ref. 21 reviews the experimental results concerned with the occurrence of the Alfvén eigenmodes in the TFTR.

Recent gyrokinetic simulations of the TAE have been reported in Refs. 22–30. Gyrokinetic toroidal code (GTC)<sup>31</sup> has been used in this paper, as the code has been successfully applied to simulations of MHD modes such as TAE,<sup>22–24</sup> reversed shear Alfvén eigenmode (RSAE),<sup>32,33</sup> beta-induced Alfvén eigenmode (BAE),<sup>34–36</sup> and geodesic acoustic mode (GAM).<sup>37,38</sup> Ref. 22 illustrates the continuum spectrum excitation by initial perturbation in cylindrical and toroidal geometries, and Ref. 23 focuses on the excitation of TAE by fast ions with the parameters of toroidal number  $n = 1$ , poloidal numbers  $m = 1, 2$ , and the safety factor  $q = 1 + 1.5r^2$ , the results of which agree well with Fu's theory.<sup>4</sup> Zhang's simulations<sup>24</sup> focus on TAE excitation by antenna and fast ions with toroidal number  $n = 5$  and poloidal numbers  $m = 7, 8$ .

<sup>a)</sup>Electronic mail: wlzh@ustc.edu.cn

Mishchenko *et al.*<sup>25–27</sup> have used the  $\delta f$  particle code GYGLES for TAE simulations and Ref. 27 interprets the transition from TAE to EPM instabilities in various parameter regions. A few other gyrokinetic simulations have focused on the kinetic effects of TAE.<sup>28,29</sup> The hybrid magnetohydrodynamics gyrokinetic code (HMGC),<sup>39</sup> wherein backgrounds are described by MHD equations and the fast ions are described by gyrokinetic equations, also focuses on simulations of TAE<sup>40</sup> and EPM.<sup>41,42</sup>

In this study, using the electromagnetic model of GTC,<sup>43</sup> we carry out gyrokinetic particle simulations of the TAE and EPM. In comparison with previous gyrokinetic simulations of TAE, our study focuses on the frequency spectrum with two components along with concentrating on the detailed mode structure and wave-particle resonance in the phase space. Further, our simulations describe the mode structure of the EPM clearly, and its difference with the TAE is discussed. In our simulations, the TAE is first excited using an antenna in order to accurately measure its frequency, growth rate, and mode structure. Subsequently, the TAE is excited by fast ions, the result of which shows that the eigenmode frequency moves towards the lower accumulation point. Further, the component of EPM in the frequency spectrum can be observed when the drive is sufficiently strong. The phase space structure of the fast ions shows that both passing and trapped particles contribute to TAE excitation and that trapped particles dominate the wave-particle resonance in our simulations. We next change the parameters of the drive strength  $R/L_{nf}$ , fast ion temperature  $T_f$ , and density  $n_f$  to study the parameters regions of TAE and EPM, and our results confirm that the frequency of the EPM is determined by the characteristic frequency of fast ion motion in a toroidal geometry. Moreover, the mode structure of the EPM can be clearly observed in our gyrokinetic simulations.

The structure of the paper is as follows. Section II presents the electromagnetic simulation model. In Sec. III, TAE excitation by antenna and fast ions are investigated. In Sec. IV, the EPM structure is presented. Section V presents the summary of this work.

## II. GYROKINETIC SIMULATION MODEL

In this section, the electromagnetic gyrokinetic simulation model used by GTC is described, and the ideal MHD equation is recovered in the long-wavelength limit. As a field perturbation can be described by Fourier decomposition in poloidal harmonics, we can derive the eigenmode equations of the coupling of the two poloidal modes in the first order.

### A. GTC formulation for electromagnetic simulation

In the GTC formulation for electromagnetic simulation, both thermal ions and fast ions are described by the gyrokinetic equation<sup>44</sup> in the inhomogeneous magnetic field, using the gyrocenter position  $\mathbf{X}$ , magnetic moment  $\mu$ , and parallel velocity  $v_{||}$ . Thus, the gyrokinetic equations with five independent variables are given as

$$(\partial_t + \dot{\mathbf{X}} \cdot \nabla + v_{||} \partial_{v_{||}}) f_\alpha(\mathbf{X}, \mu, v_{||}) = 0, \quad (1)$$

$$\dot{\mathbf{X}} = v_{||} \frac{\mathbf{B}_0 + \delta\mathbf{B}}{B_0} + \frac{c\mathbf{b}_0 \times \nabla\phi}{B_0} + \frac{v_{||}^2}{\Omega} \nabla \times \mathbf{b}_0 + \frac{\mu}{m\Omega} \mathbf{b}_0 \times \nabla B_0, \quad (2)$$

$$v_{||} = -\frac{1}{m} \frac{\mathbf{B}_0 + \frac{B_0 v_{||}}{\Omega} \nabla \times \mathbf{b}_0 + \delta\mathbf{B}}{B_0} \cdot (\mu \nabla B_0 + Z \nabla \phi) - \frac{Z}{m_\alpha c} \partial_t A_{||}. \quad (3)$$

Here, the index  $\alpha = e, i, f$  denotes the particle species (electron, thermal ion, and fast ion),  $Z_\alpha$  denotes the particle charge,  $m_\alpha$  denotes the particle mass,  $\Omega$  denotes the thermal ion cyclotron frequency,  $\delta\mathbf{B}$  and  $\phi$ , respectively, denote the perturbed magnetic field and electrostatic potentials, and  $\mathbf{B}_0 = B_0 \mathbf{b}_0$  denotes the equilibrium magnetic field. In our description, we exclude the compressional component of the magnetic field perturbation by assuming  $\delta B_{||} = 0$ , and thus, we obtain

$$\delta\mathbf{B} = \delta\mathbf{B}_\perp = \nabla \times \lambda \mathbf{B}_0, \quad (4)$$

with  $\lambda = A_{||}/B_0$ . All the perturbed quantities such as  $\phi$  and  $A_{||}$  are gyrophase-averaged for the thermal ions and fast ions. The electrons are treated as equivalent to fluid in the lowest order with adiabatic approximation, and the higher-order nonadiabatic terms are treated kinetically with all nonlinear effects preserved.<sup>43,45</sup> However, only the linear terms are preserved in this study. The electron continuity equation is derived from integration of Eq. (1) in the velocity space and the terms up to the first order are retained in the perturbation

$$\partial_t \delta n_e + \mathbf{B}_0 \cdot \nabla \left( \frac{n_0 \delta u_{||e}}{B_0} \right) + B_0 \mathbf{v}_E \cdot \nabla \left( \frac{n_0}{B_0} \right) - n_0 (\delta \mathbf{v}_* + \mathbf{v}_E) \cdot \frac{\nabla B_0}{B_0} + \delta\mathbf{B} \cdot \nabla \left( \frac{n_0 u_{||0}}{B_0} \right) = 0, \quad (5)$$

where  $\delta n_e$  denotes the perturbed electron density,  $\mathbf{v}_E = c\mathbf{b}_0 \times \nabla\phi/B_0$ ,  $\delta \mathbf{v}_* = \mathbf{b}_0 \times \nabla(\delta P_{||} + \delta P_\perp)/(n_0 m_e \Omega_e)$ ,  $\delta P_\perp = \int dv \mu B_0 \delta f$  and  $\delta P_{||} = \int dv m v_{||}^2 \delta f$ . The electron parallel fluid velocity can be calculated by using the gyrokinetic Ampère's law as

$$n_0 e \delta u_{||e} = \frac{c}{4\pi} \nabla_\perp^2 \delta A_{||} + n_{0i} e Z_i \delta u_{||i} + n_{0f} e Z_f \delta u_{||f}, \quad (6)$$

where  $\delta u_{||i}$  and  $\delta u_{||f}$ , respectively, denote the parallel flow velocity of the thermal ions and fast ions.

The inductive potential is defined as  $\delta\phi_{ind} = \delta\phi_{eff} - \delta\phi$ , where  $\delta\phi_{eff}$  denotes the effective potential corresponding to the parallel electric field. Consequently, the vector potential can be written as the following equation:

$$\frac{\partial \delta A_{||}}{\partial t} = c \mathbf{b}_0 \cdot \nabla \delta\phi_{ind}. \quad (7)$$

The value of  $\delta\phi_{eff}$  is derived from the expression  $e\delta\phi_{eff}/T_e = \delta n_e/n_0$  in the lowest order. This system can be closed by the gyrokinetic Poisson's equation

$$\frac{Z_i^2 n_i}{T_i} (\phi - \tilde{\phi}) = \sum_{\alpha=e,i,f} Z_\alpha \delta n_\alpha, \quad (8)$$

where  $\tilde{\phi}$  denotes the second gyrophase-averaged electrostatic potential expressed as  $\tilde{\phi}(\mathbf{x}) = \sum_k \phi_k \Gamma_0(k_\perp^2 \rho_i^2) \exp(i\mathbf{k} \cdot \mathbf{x})$ .

## B. MHD limit and eigenmode equations

In the ideal MHD limit,  $\phi_{eff} = 0$  upon assuming  $\omega_* \ll k_\parallel V_A$ , and therefore, the continuity equation (5) can be written as

$$\partial_t \delta n_e + \mathbf{B}_0 \cdot \nabla \left( \frac{n_0 \delta u_{\parallel e}}{B_0} \right) - n_0 \mathbf{v}_E \cdot \frac{\nabla B_0}{B_0} = 0. \quad (9)$$

The Poisson equation (8) in the long-wavelength limit becomes

$$\frac{c^2}{4\pi e} \nabla_\perp \left( \frac{1}{v_A^2} \right) \nabla_\perp \phi = \delta n_e. \quad (10)$$

Applying the  $\nabla_\perp^2$  operator to Eq. (7) yields

$$\frac{1}{c} \frac{\partial}{\partial t} (\nabla_\perp^2 A_{\parallel}) = -\mathbf{b}_0 \cdot \nabla (\nabla_\perp^2 \phi). \quad (11)$$

Ampère's law, given by Eq. (6), yields

$$\delta u_{\parallel e} = c \frac{e}{T_e} \lambda_D^2 (\nabla_\perp^2 A_{\parallel}). \quad (12)$$

Based on Eqs. (9)–(12), the dispersion relation can be written as

$$\omega^2 \nabla_\perp \left( \frac{1}{v_A^2} \nabla_\perp \phi \right) = -B_0 \mathbf{b}_0 \cdot \nabla \left[ \frac{1}{B_0} \nabla^2 (\mathbf{b}_0 \cdot \nabla \phi) \right], \quad (13)$$

which recovers the ideal MHD equations. The wave field perturbation with frequency  $\omega$  can be described by a Fourier decomposition in poloidal harmonics as

$$\phi(r, \theta, \zeta, t) = \sum_m \phi_m(r) \exp(-im\theta + in\zeta - i\omega t). \quad (14)$$

In toroidal geometry, the magnetic field strength is  $\mathbf{B} \approx \mathbf{B}_0(1 - \epsilon x \cos \theta)$ , the radius is normalized by  $x = r/a$ , and the inverse aspect ratio is defined as  $\epsilon = a/R$ . Expanding the toroidicity effects to the first order and retaining only two dominant poloidal modes, we obtain the following coupled eigenmode equations:

$$\left[ \frac{d}{dr} r^3 \left( \frac{\omega^2}{v_A^2} - k_{\parallel m}^2 \right) \frac{d}{dr} - (m^2 - 1) r \left( \frac{\omega^2}{v_A^2} - k_{\parallel m}^2 \right) \right] \phi_m + \left( \frac{3}{2} \epsilon \frac{d}{dr} \frac{\omega^2 r^4}{v_A^2 a} \frac{d}{dr} \right) \phi_{m+1} = 0, \quad (15)$$

$$\left[ \frac{d}{dr} r^3 \left( \frac{\omega^2}{v_A^2} - k_{\parallel m+1}^2 \right) \frac{d}{dr} - [(m+1)^2 - 1] r \left( \frac{\omega^2}{v_A^2} - k_{\parallel m+1}^2 \right) \right] \phi_{m+1} + \left( \frac{3}{2} \epsilon \frac{d}{dr} \frac{\omega^2 r^4}{v_A^2 a} \frac{d}{dr} \right) \phi_m = 0. \quad (16)$$

In the limit of cylindrical geometry ( $\epsilon = 0$ ), the two poloidal modes  $\phi_m$  and  $\phi_{m+1}$  are decoupled and Eqs. (15) and (16) are singular at  $\omega_1^2 = k_{\parallel}^2 v_A^2$ ; this singularity yields the two cylindrical shear Alfvén continua. In toroidal geometry, the two poloidal modes are coupled ( $\epsilon \neq 0$ ) due to finite toroidicity and two following branches of the toroidal continuum can be derived from Eq. (15) and Eq. (16) by setting the determinant of the coefficient of the second-order derivative terms to zero.<sup>4</sup> The toroidal continuum is given by

$$\omega_\pm^2 = \frac{4k_{\parallel m}^2 v_A^2 + 4k_{\parallel m+1}^2 v_A^2 \pm 4\sqrt{(k_{\parallel m}^2 v_A^2 - k_{\parallel m+1}^2 v_A^2)^2 + 9\epsilon^2 x^2 k_{\parallel m}^2 v_A^2 k_{\parallel m+1}^2 v_A^2}}{2 - 9\epsilon^2 x^2}. \quad (17)$$

The TAE exists in the gap whose width is given by

$$\Delta\omega = \omega_+ - \omega_- \cong 2q\chi(|k_{\parallel m} v_A|)_{q=(m+1/2)/n}, \quad (18)$$

and the frequency of the eigenmode lies between the two continuum spectra.

## III. GTC SIMULATION OF TAE EXCITATION

### A. TAE excitation by antenna

In this subsection, we discuss TAE excitation by antenna, which provides an accurate method to determine the eigenfrequency, growth rate, and mode structure. In our simulations, the inverse aspect ratio of tokamak is  $\epsilon = 0.3$  and the safety factor is  $q = 1.2886 + 0.8(\psi/\psi_w) - 0.4(\psi/\psi_w)^2$ , where  $\psi$  denotes the poloidal flux and  $\psi_w = \psi(r=a)$ . Thus, the safety factor  $q = 1.5$  and the magnetic shear has a value 0.2 at the  $r = 0.5a$  position. The simulations are all linear and we

apply a toroidal mode filter to select only the  $n = 5$  toroidal mode. In toroidal geometry, the two poloidal modes couple at the center of two rational surfaces, where the parallel wave number is  $k_\parallel = 1/(2qR)$  and the safety factor is  $q = (m + 1/2)/n$ . We can define  $\omega_A = V_A/(2qR)$  as a unit of frequency in our simulations. Fig. 1 shows the continuum spectrum of the  $m = 7$  and  $m = 8$  harmonic coupling obtained using a code called ALCON<sup>33</sup> to solve the ideal Alfvén continuum equations, where the lower and upper accumulation points are  $0.800\omega_A$  and  $1.200\omega_A$ , respectively. In our gyrokinetic simulations, TAE excitation by antenna is the first step. The computation mesh consists of 16 parallel grids and 64 radial grids. The number of poloidal grids is 32 in the innermost surface and 128 in the outermost surface, and therefore, the total number of grids on a poloidal plane is 8385. The antenna is implemented through an extra synthetic potential  $\delta\phi_{ant}$  added to the inductive potential  $\delta\phi_{ind}$  in the GTC,

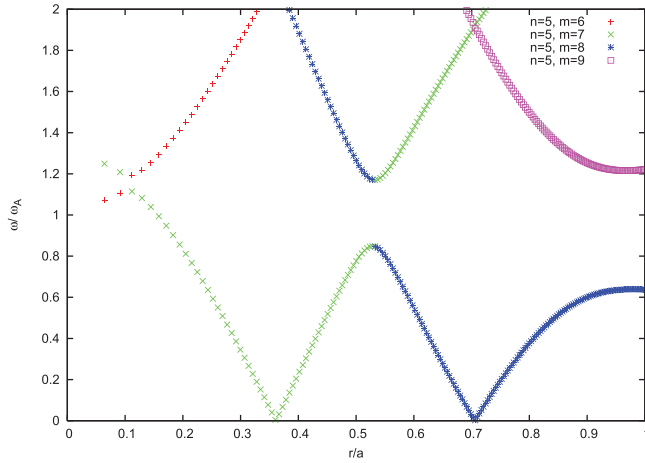


FIG. 1. Alfvén continuum spectrum of the  $n=5$  mode in the ideal MHD limit.

$$\delta\phi_{ind} = \delta\phi_{eff} - \delta\phi + \delta\phi_{ant}, \quad (19)$$

and the potential  $\delta\phi_{ant}$  is implemented in the form of a potential perturbation

$$\begin{aligned} \delta\phi_{ant} = \delta\phi_{ant}(\hat{\Psi}) & [\cos(m\theta - n\zeta) \\ & + \cos((m+1)\theta - n\zeta)] \cos(\omega_{ant}t). \end{aligned} \quad (20)$$

Here,  $\delta\phi_{ant}(\hat{\Psi})$  represents the profile of a small perturbation along the radial direction, with its maximum located at  $r = 0.5a$ , and it decays exponentially to zero at the inner and outer boundaries. The time history plot in Fig. 2 shows that the mode amplitude grows linearly with time when  $\omega_{ant} = \omega_A$  and the two lines with black and red colors represent the real and imaginary parts of the amplitude. The frequency spectra can be obtained by performing a fast Fourier transform (FFT) of the time series. Fig. 3 shows the corresponding frequency spectra obtained when the driving frequency is varied. We first set the drive frequency  $\omega_{ant} = \omega_A$ , as shown in Fig. 3(a), and the spectrum shows the existence of only one component since the antenna and eigenmode have the same frequency. However, when the frequencies are set to  $\omega_{ant} = 0.400\omega_A$  and  $\omega_{ant} = 1.500\omega_A$ , all of the frequencies at the lower and upper accumulation points and the eigenmode are observed, as shown in Figs. 3(b) and 3(c). From these figures, it is

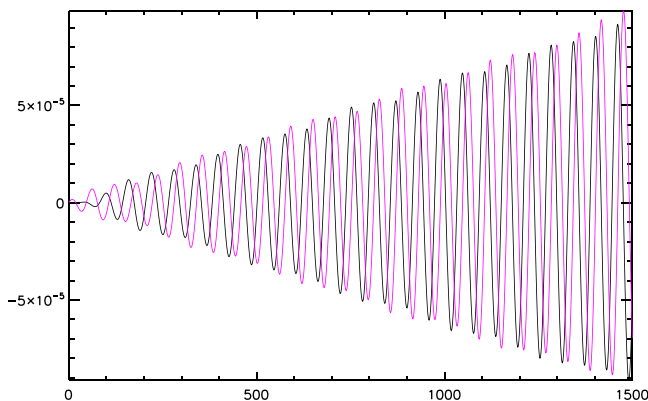


FIG. 2. Time history of vector potential  $A_{||}$  with  $n=5$  and  $m=7$  when the TAE is excited by antenna.

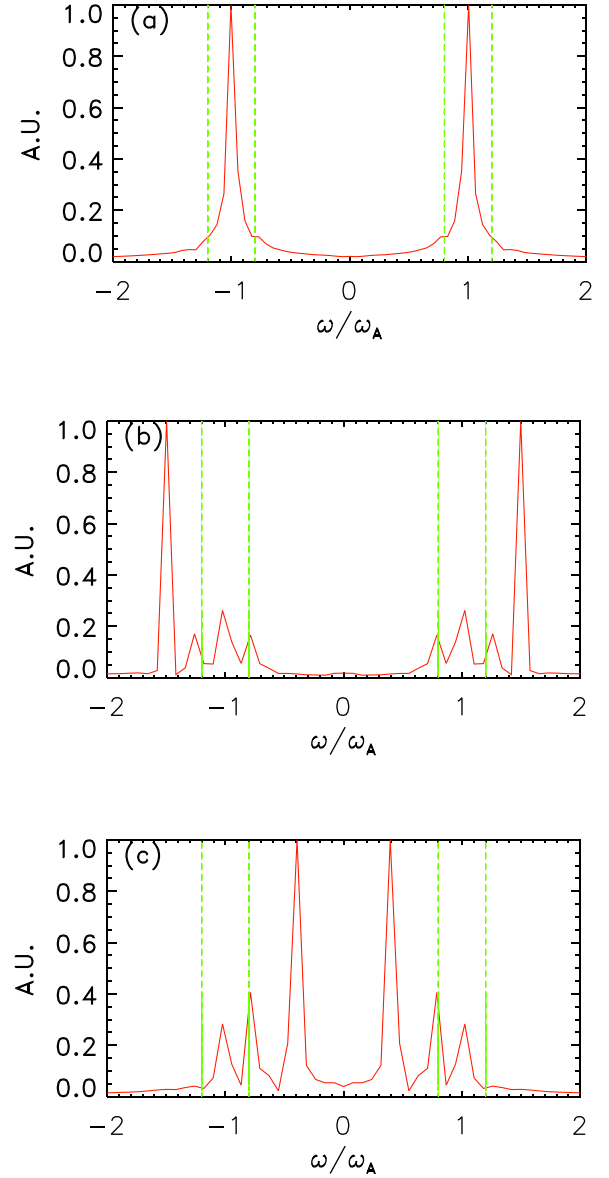


FIG. 3. Frequency spectrum of  $A_{||}$  when the drive frequency scans from  $0.400\omega_A$  to  $1.500\omega_A$ . (a) Frequency spectrum obtained when drive frequency is equal to the TAE frequency. (b) The drive frequency is  $\omega_{ant} = 1.500\omega_A$ . (c) The drive frequency is  $\omega_{ant} = 0.400\omega_A$ . The green lines indicate the lower and upper bounds of the continuum.

obvious that the frequencies of the upper accumulation point, the lower accumulation point, and the eigenmode are  $1.200\omega_A$ ,  $0.800\omega_A$ , and  $\omega_A$ , and these values agree well with the continuum spectrum shown in Fig. 1. The mode structure of  $\phi$  and  $A_{||}$  are shown in Fig. 4 for TAE excitation by antenna. The radial mode structure shows a clear symmetry as an MHD mode and  $m = 7, 8$  are the dominant poloidal harmonics.

## B. TAE excitation by fast ions

In this section, we discuss the gyrokinetic simulations of TAE excitation by fast ions. From Fu's theory,<sup>46</sup> the growth rate  $\gamma$  of TAE excitation by fast ions can be expressed as

$$\frac{\gamma}{\omega_{TAE}} = q^2 \beta_f \left( \frac{\omega_*}{\omega_{TAE}} - 1 \right) f_r - \frac{\gamma_d}{\omega_{TAE}}, \quad (21)$$

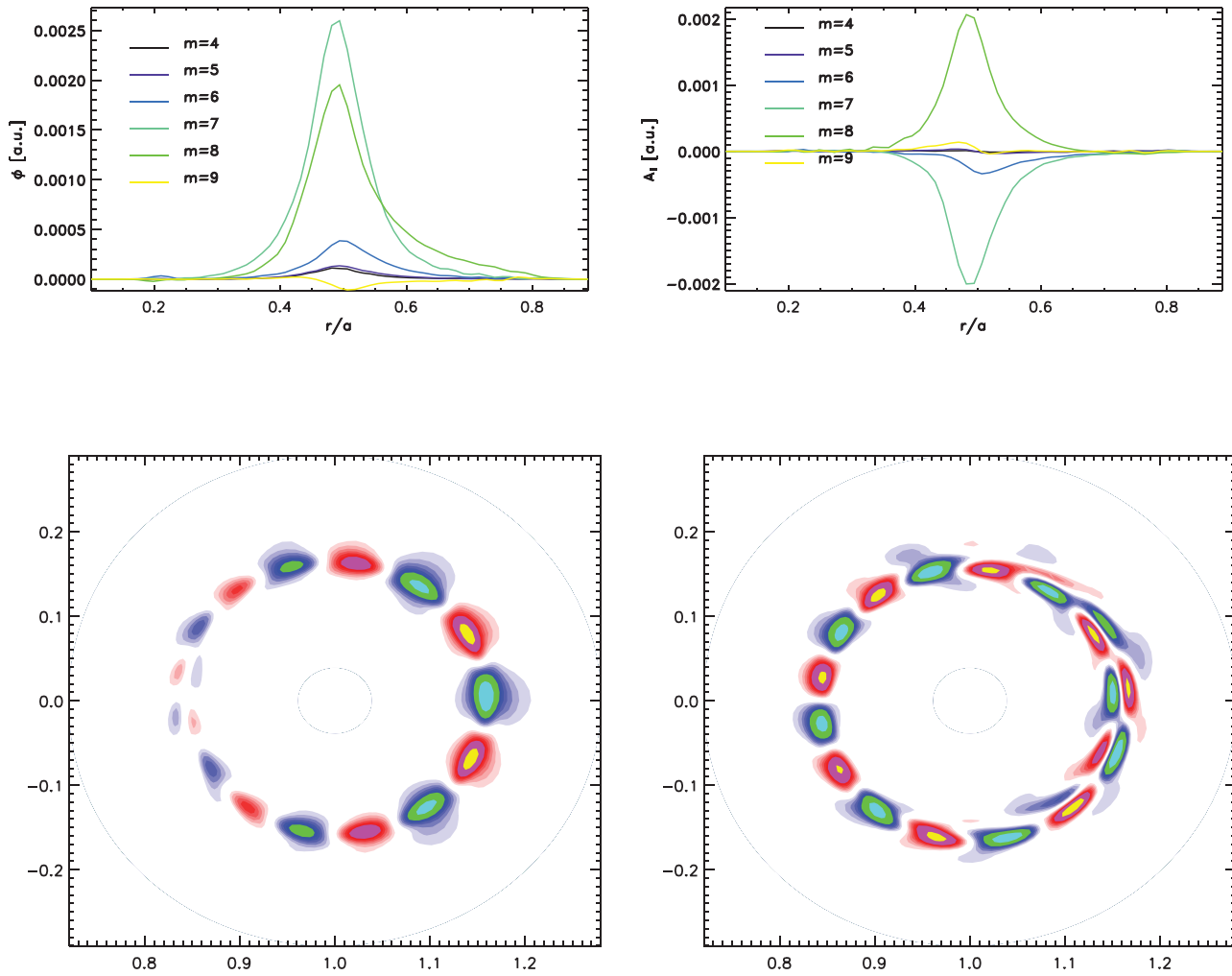


FIG. 4. Radial (upper panels) and poloidal (lower panels) mode structures of  $\phi$  (left) and  $A_{\parallel}$  (right) for TAE excitation by antenna.

where  $\beta_f$  denotes the fast ion beta value,  $\omega_* = k_{\theta} \rho_f V_{tf} / L_{nf}$  denotes the diamagnetic drift frequency of fast ions,  $f_r$  denotes the fraction of the number of resonant particles,  $\gamma_d$  denotes the growth rate of the TAE due to thermal plasma kinetic effects and continuum damping, and  $\omega_{TAE}$  represents the frequency of TAE. From Eq. (21), we note that TAE excitation by fast ions should satisfy at least three conditions. First, wave-particle resonance should occur. The resonance condition of passing particles is  $l\omega_t = \omega_{TAE}$  and the trapped particles resonance can be expressed as the bounce-precession resonance  $n\omega_{pre} + l\omega_b = \omega_{TAE}$ , where  $\omega_t$  denotes the transit frequency,  $\omega_b$  denotes the bounce frequency,  $\omega_{pre}$  denotes the precession frequency of fast ions, and  $l$  represents an integer number. As predicted by Chen's theory,<sup>6,7</sup>  $V_{tf} = V_A$  and  $V_{tf} = \frac{1}{3}V_A$  are the two resonance points of the wave-particle interaction. Here,  $V_{tf} = \sqrt{T_f/m_f}$  denotes the thermal speed of the fast ions. Consequently, the diamagnetic drift frequency of fast ions, as a source of free energy, should be sufficiently large to allow inverse Landau damping to occur. When the equilibrium parameters are chosen, the diamagnetic drift frequency  $\omega_*$  is determined by  $R/L_{nf}$ , which is the profile of the fast ions density gradient. Finally, the mode must overcome the damping of thermal plasma, such as continuum damping, Landau damping, and radiative damping.

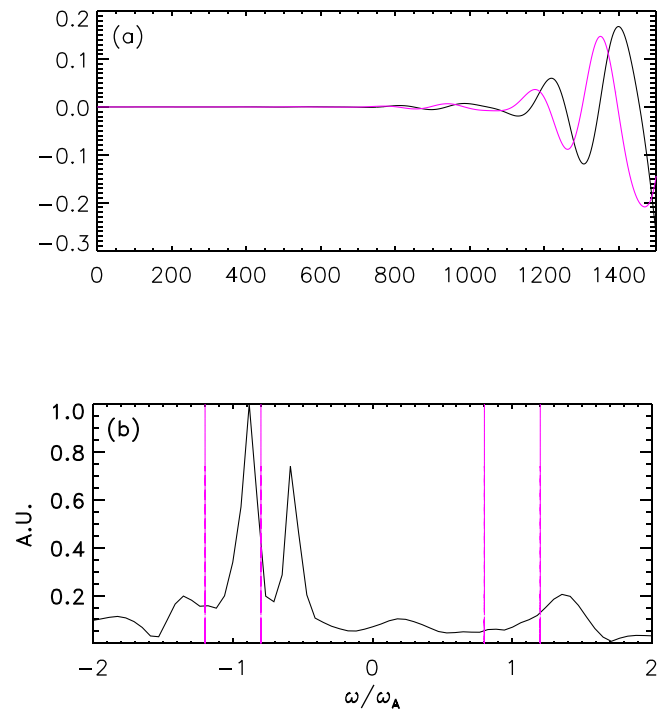


FIG. 5. (a) Time history of vector potential  $A_{\parallel}$  with  $n=5, m=7$  when the TAE is excited by fast ions. (b) Frequency spectrum of  $A_{\parallel}$  where the dominant frequency is that of the TAE. The weaker component corresponds to the EPM.

In our simulations, the equilibrium parameters are set to  $R_0 = 70.97$  cm,  $\epsilon = 0.3$ ,  $B_0 = 19\,100$  Gauss,  $T_e = T_i = 2500$  eV, and  $n_e = n_i = 4.525 \times 10^{14}$  /cm<sup>3</sup>. These simulations evolved  $4 \times 10^6$  thermal ions and fast ions over 2000 time steps. From these parameters, the Alfvén speed is  $V_A = \sqrt{B^2/4\pi n_i m_p} = 1.96 \times 10^8$  cm/s, the thermal speeds of the fast ion  $V_{tf} = \sqrt{T_f/m_p} = 1.96 \times 10^8$  cm/s, when  $T_f = 16T_i$ . Therefore, the fast ion energy in this case satisfies the resonance point of  $V_{tf} = V_A$ . All the three species are loaded with the Maxwell distribution, and the other parameters are set as  $n_f = 0.07n_i$ ,  $a = 80\rho_f$ , and  $\beta_e = 4\pi n_0 T_e / B_0^2 = 0.125$  on the magnetic axis. The maximum density gradient of fast ions is  $R/L_{nf} = 62.2$ , located at the  $r = 0.5a$  surface where the safety factor  $q = 1.5$ . Fig. 5(a) shows the linear growth of amplitude of the TAE excited by fast ions; the two lines represent its real and imaginary parts similar to the notation followed in Fig. 2. Fig. 5(b) shows the corresponding frequency spectra. From Fig. 5(b), we note that the dominant TAE frequency is  $\omega = 0.880\omega_A$  which moves towards lower accumulation point when compared with the dominant frequency in the case of antenna excitation. The weaker component in the spectrum is the EPM frequency, which is discussed in detail in Sec. IV. The mode structure of the TAE excited by fast ions shows a clear radial symmetry breaking (Fig. 6), which is due to the

non-perturbative kinetic effects of fast ions.<sup>33</sup> Moreover, this radial structure of the TAE indicates that  $m=7$  and  $m=8$  are the dominant modes. The phase space structure in Fig. 7 confirms the theoretical prediction that both passing and trapped particles can contribute to wave-particle resonance. The pitch angle of the passing particles is greater in terms of absolute number, and the trapped particles resonate with the TAE in the region with a smaller absolute value of the pitch angle. The solid lines in Fig. 7 indicate the transit resonance of passing particles with harmonics  $l=1,2,3$ . The resonance is strongest near the region of  $T_f = 5T_i$ , and it is very weak when the fast ion energy exceeds  $20T_i$ . Based on the resonance strength and the size of resonance island, we can conclude that trapped particles dominate the wave-particle resonance in our simulations. However, the type of particles dominating the wave-particle resonance may depend on the experimental apparatus used as the heating methods are different for different experimental setups.

#### IV. GLOBAL GYROKINETIC PARTICLE SIMULATION OF EPM

It is well known that TAE as weakly damped gap modes can be destabilized; however, EPM can only be observed

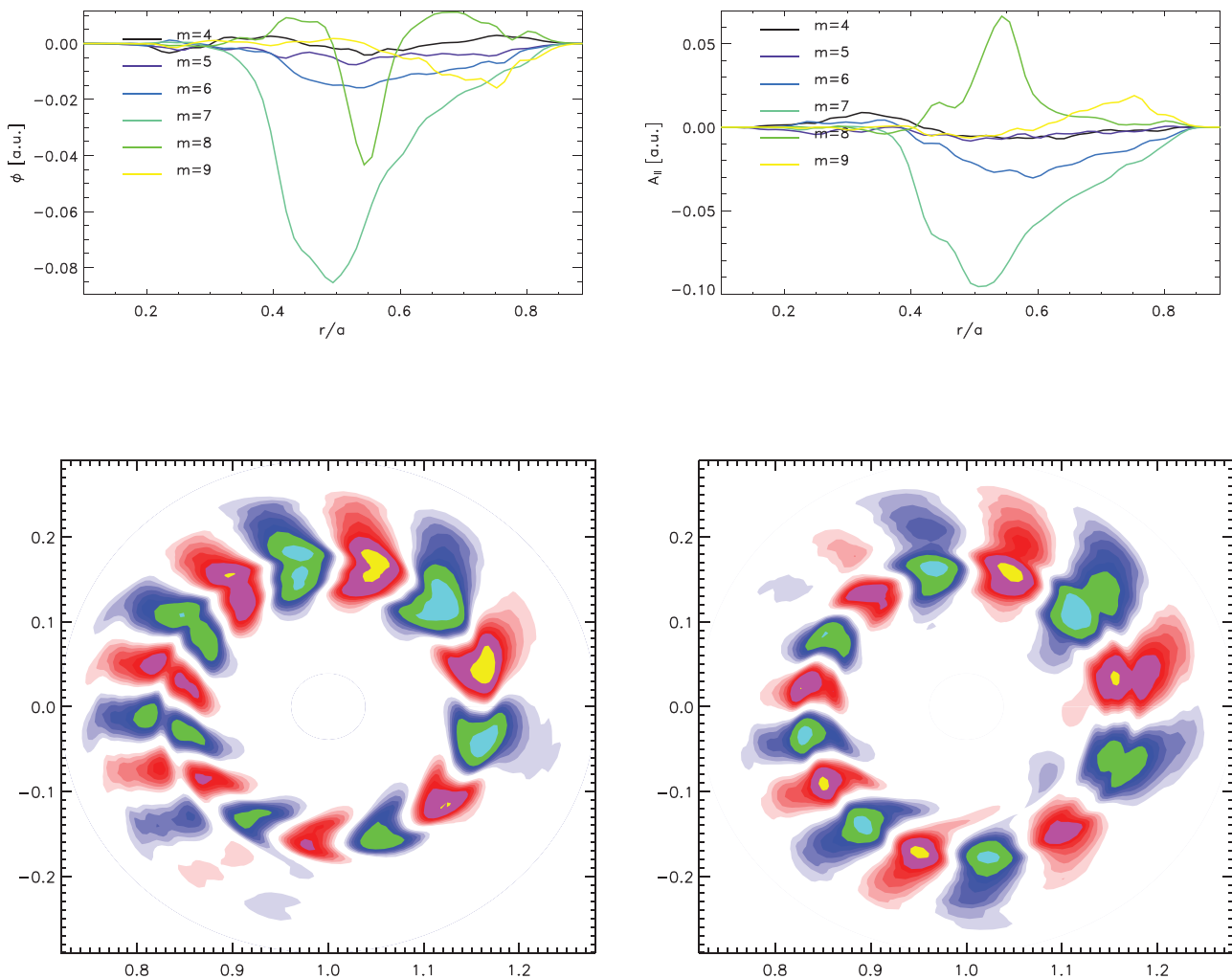


FIG. 6. Radial (upper panels) and poloidal (lower panels) mode structures of  $\phi$  (left) and  $A_{\parallel}$  (right) for TAE excitation by fast ions.

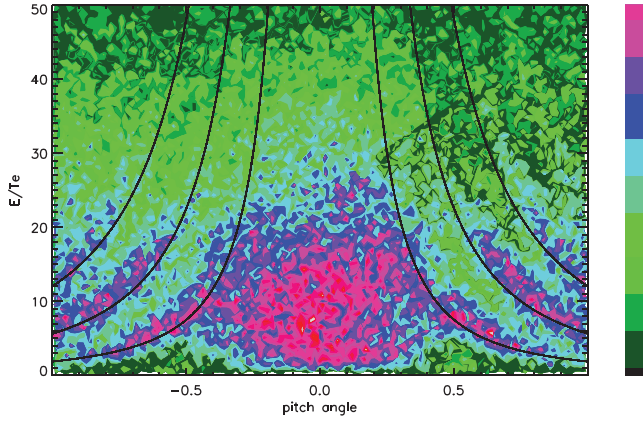


FIG. 7.  $\delta f^2$  as a function of particle energy  $E/T_e$  and pitch angle  $\lambda = v_{\parallel}/v$ . The solid lines from top to bottom indicate the points satisfying the resonance condition  $\omega_{TAE} = l\omega_r$  with the harmonic  $l = 1, 2, 3$ .

when the mode drive is sufficiently strong to overcome the continuum damping. The term  $-i\Lambda$  in the fishbone-like dispersion relation  $-i\Lambda + \delta W_f + \delta W_k = 0$  represents the mode frequency shift from the accumulation points for TAE, and it denotes continuum damping in the case of EPM. The frequency of the EPM is determined by the characteristic frequencies of fast ion motions such as bounce, transit, and precession frequencies in toroidal geometry, which always locate close to the lower or upper of the continuum spectrum. At the same time, the growth rate of the EPM is also determined by the motions of fast ions. The real frequency of the EPM near marginal stability is

$$\text{Re}\delta W_k(\omega_r) + \delta W_f = 0, \quad (22)$$

and the growth rate is

$$\frac{\gamma}{\omega_r} = (-\omega_r \partial_{\omega_r} \text{Re}\delta W_k)^{-1} (\text{Im}\delta W_k - \Lambda). \quad (23)$$

It is interesting to study the parametric dependencies of the mode. We observe a continuous modification of the TAE into EPM that is caused by varying the fast ion parameters such as density, density gradient, and energy. The mode growth rate dependence on the fast ion density gradient is shown in the upper panel of Fig. 8, and the parameter regions of the TAE and EPM are distinguished by the dashed line. The TAE shows a clear mode structure when  $R/L_{nf}$  is chosen near the critical value, as shown in Fig. 8. In this case, all the parameters are the same as those in the case of TAE excitation by fast ions except the density gradient. It is obvious that the TAE is excited with a weak drive while the EPM is excited with a stronger drive. The mode structure is not clear in the parameter regions near the transition region due to continuum damping. In our simulation of TAE excitation with  $R/L_{nf} = 62.2$ , the TAE coexists with a weaker EPM, as shown in Fig. 5(b). Such a two-component spectrum has not thus far received any attention from other researchers. Therefore, distinguishing the parameters regions of TAE and EPM may be useful in analyzing experimental data. The lower panel of Fig. 8 shows the energy scan of the growth rate, and the plot indicates that the growth rate is not a monotonic function of the fast ion energy. As the fast ion energy

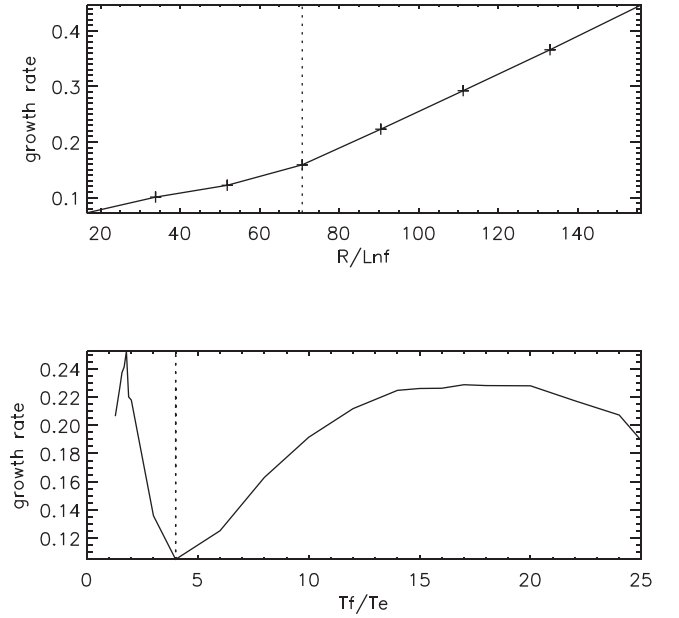


FIG. 8. Upper panel: Growth-rate dependence of the drive strength. The dashed line indicates the critical transition point between the TAE and EPM, as the TAE exists under relatively the weaker drive conditions while the EPM is observed for a stronger drive. Lower panel: The growth-rate dependence on the fast ion energy when the drive is sufficiently strong. The EPM exists in the lower fast ion energy region.

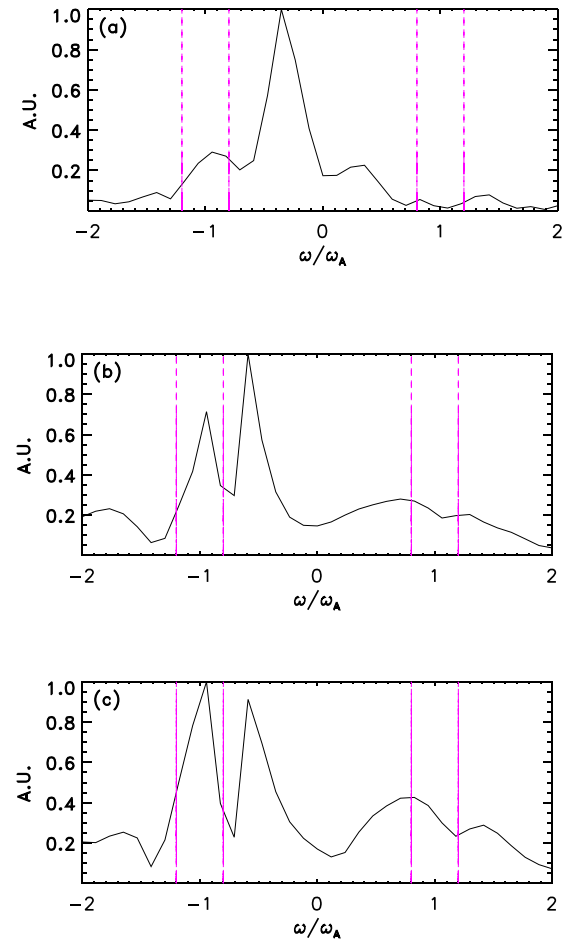


FIG. 9. Frequency spectrum of  $A_{\parallel}$  for varying fast ion energy. (a) Only the EPM is observed when  $T_f = 1.78T_e$ . (b) Weak TAE coexists with EPM when  $T_f = 16T_e$ . (c) A stronger TAE coexists with EPM when  $T_f = 20T_e$ . The dashed lines denote the frequency range of the continuum spectrum.

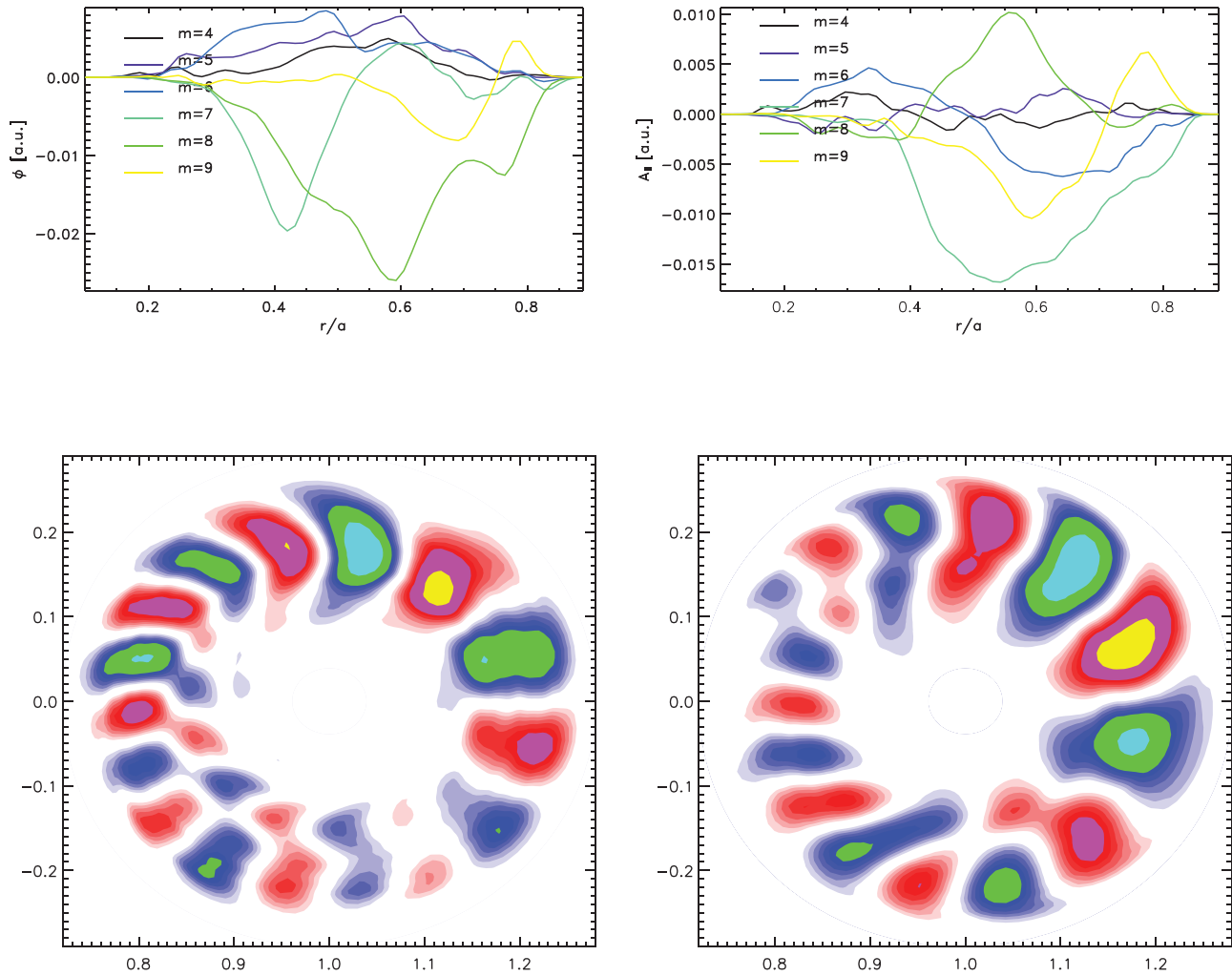


FIG. 10. Mode structure of EPM. Radial (upper panels) and poloidal (lower panels) mode structures are shown. The right hand image is obtained using the data of the electrostatic potential  $\phi$  and the left hand image is obtained using the data of the vector potential  $A_{||}$ .

is increased stepwise, the density corresponding varies in the opposite direction such that keep the parameter  $\beta_f$  remains constant. In this figure,  $T_f = 1.78T_e$  and  $T_f = 16T_e$  indicate the two peaks of mode growth rate; in fact, these two points are the resonance points  $V_{if} = V_A/3$  and  $V_{if} = V_A$  corresponding to the fast ion resonance with TAE. Fig. 9 shows the plot of the frequency spectrum when the fast ion energy is varied. Only the EPM is observed in the lower fast ion energy region  $T_f = 1.78T_e$  in Fig. 9(a) and the weak TAE spectrum coexists with the EPM (Fig. 9(b)) for  $T_f = 16T_e$ . In Fig. 9(c), with  $T_f = 20T_e$ , the fast ion energy is so large that the strength of the TAE exceeds that of the EPM. This result validates the demarcation of the parameters regions of TAE and EPM in the lower panel of Fig. 8. From all the three plots shown in Fig. 9, we conclude that the frequency of the EPM is determined by the characteristic frequencies of fast ion motion in toroidal geometry as the frequency moves towards the lower accumulation point with increasing fast ion energy. The frequency of the TAE does not change significantly because it is determined by background plasmas. Besides, the frequency of the EPM does not exceed the lower bound of the continuum upon varying the fast ion energy because of the effects of continuum damping. Fig. 10 shows

the mode structure of the EPM with fast ion energy  $T_f = 4T_e$ . The poloidal mode structure of the EPM shows the feature of an MHD mode, which is different from the radial symmetry break observed for TAE excitation by fast ions. The radial width of the EPM mode structure is larger than that of the TAE.

## V. SUMMARY

In summary, we successfully performed global gyrokinetic particle simulations of TAE and EPM. Further, the differences between TAE and EPM were discussed. In our simulations, the frequency, growth rate, and mode structure of the TAE were measured. TAE excitation by antenna provides a method to precisely measure the eigenmode frequency, growth rate, and mode structure of the TAE. The fast ion excitation leads to a significant radial symmetry breaking of the TAE mode structure relative to ideal MHD mode due to non-perturbative contributions of fast ions, and consequently, the frequency of the TAE moves to the lower region of the continuum. The phase space structure of fast ions shows that both passing particles and trapped particles can contribute to TAE excitation; however, trapped particles

dominate the wave-particle resonance in our simulations. The comparison of the TAE and EPM shows that these two modes can coexist in certain parameter regions. The frequency of the EPM is determined by the characteristic frequencies of fast ion motion in toroidal geometry, and the frequency of TAE does not vary significantly because this frequency is determined by background plasmas. In this work, we measured the frequency, growth rate, and mode structure of the EPM. Through our analysis of the simulation results, we distinguished the TAE and EPM clearly, and we confirmed that the gyrokinetic particle-in-cell code can accurately simulate the Alfvén eigenmodes in toroidal geometry.

## ACKNOWLEDGMENTS

This work was supported by the National Natural Science Foundation of China, the National Basic Research Program of China, and the National Special Research Program of China for ITER. Simulations were performed on supercomputers at NSCC-TJ.

- <sup>1</sup>See <http://www.iter.org> for information about ITER.
- <sup>2</sup>C. Z. Cheng, L. Chen, and M. S. Chance, *Ann. Phys.* **161**, 21 (1985).
- <sup>3</sup>G. Y. Fu and C. Z. Cheng, *Phys. Fluids B* **2**, 985 (1990).
- <sup>4</sup>G. Y. Fu and J. W. V. Dam, *Phys. Fluids B* **1**, 1949 (1989).
- <sup>5</sup>M. N. Rosenbluth and P. H. Rutherford, *Phys. Rev. Lett.* **34**, 1428 (1975).
- <sup>6</sup>S.-T. Tsai and L. Chen, *Phys. Fluids B* **5**, 3284 (1993).
- <sup>7</sup>L. Chen, *Phys. Plasmas* **1**, 1519 (1994).
- <sup>8</sup>F. Zonca and L. Chen, *Phys. Plasmas* **3**, 323 (1996).
- <sup>9</sup>F. Zonca and L. Chen, *Phys. Plasmas* **7**, 4600 (2000).
- <sup>10</sup>F. Zonca, S. Briguglio, L. Chen, S. Dettrick, G. Fogaccia *et al.* *Phys. Plasmas* **9**, 4939 (2002).
- <sup>11</sup>G. Y. Fu, C. Z. Cheng, R. Budny, Z. Chang, D. S. Darrow, E. Fredrickson, E. Mazzucato, R. Nazikian, and S. Zweben, *Phys. Rev. Lett.* **75**, 2336 (1995).
- <sup>12</sup>E. M. Carolipio, W. W. Heidbrink, C. Z. Cheng, M. S. Chu, G. Y. Fu, A. Jaun, D. A. Spong, A. D. Turnbull, and R. B. White, *Phys. Plasmas* **8**, 3391(2001).
- <sup>13</sup>S. A. Arshad and D. J. Campbell, *Plasma Phys. Controlled Fusion* **37**, 715 (1995).
- <sup>14</sup>H. Kimura, Y. Kusama, M. Saigusa *et al.* *Nucl. Fusion* **38**, 1303 (1998).
- <sup>15</sup>K. Shinohara, Y. Kusama, M. Takechi *et al.* *Nucl. Fusion* **41**, 603 (2001).
- <sup>16</sup>A. Weller, D. A. Spong, R. Jaenicke, A. Lazaros, F. P. Penningfeld, and S. Sattler, *Phys. Rev. Lett.* **72**, 1220 (1994).
- <sup>17</sup>A. Weller, M. Anton, J. Geiger, M. Hirsch, R. Jaenicke, A. Werner, C. Nührenberg, and E. Sallander, *Phys. Plasmas* **8**, 931 (2001).
- <sup>18</sup>L. Chen and F. Zonca, *Nucl. Fusion* **47**, s727 (2007).
- <sup>19</sup>G. Vlad, F. Zonca, and S. Briguglio, *Riv. Nuovo Cimento* **22**, 1 (1999).
- <sup>20</sup>W. W. Heidbrink, *Phys. Plasmas* **15**, 055501 (2008).
- <sup>21</sup>K. L. Wong, *Plasma Phys. Controlled Fusion* **41**, R1 (1999).
- <sup>22</sup>Y. Nishimura, Z. Lin, and W. X. Wang, *Phys. Plasmas* **14**, 042503 (2007).
- <sup>23</sup>Y. Nishimura, *Phys. Plasmas* **16**, 030702 (2009).
- <sup>24</sup>W. Zhang, I. Holod, Z. Lin, and Y. Xiao, *Phys. Plasmas* **19**, 022507 (2012).
- <sup>25</sup>A. Mishchenko, R. Hatzky, and A. Könies *Phys. Plasmas* **11**, 5480 (2004).
- <sup>26</sup>A. Mishchenko, A. Könies, and R. Hatzky, *Phys. Plasmas* **15**, 112106 (2008).
- <sup>27</sup>A. Mishchenko, A. Könies, and R. Hatzky, *Phys. Plasmas* **16**, 082105 (2009).
- <sup>28</sup>P. Lauber, S. Gunter, and S. D. Pinches, *Phys. Plasmas* **12**, 122501 (2005).
- <sup>29</sup>J. Lang, Y. Chen, S. E. Parker, and G. Y. Fu, *Phys. Plasmas* **16**, 102101 (2009).
- <sup>30</sup>E. M. Bass and R. E. Waltz, *Phys. Plasmas* **17**, 112319 (2010).
- <sup>31</sup>Z. Lin, T. S. Hahm, W. W. Lee, W. M. Tang, and R. B. White, *Science* **281**, 1835 (1998).
- <sup>32</sup>W. Deng, Z. Lin, I. Holod, X. Wang, Y. Xiao, and W. Zhang, *Phys. Plasmas* **17**, 112504 (2010).
- <sup>33</sup>W. Deng, Z. Lin, and I. Holod, *Nucl. Fusion* **52**, 043006 (2012).
- <sup>34</sup>H. Zhang, Z. Lin, I. Holod, X. Wang, Y. Xiao, and W. Zhang, *Phys. Plasmas* **17**, 112505 (2010).
- <sup>35</sup>H. Zhang, Z. Lin, and I. Holod, *Phys. Rev. Lett.* **109**, 025001 (2012).
- <sup>36</sup>H. Zhang, Z. Lin, W. Deng, I. Holod, Z. X. Wang, Y. Xiao, and W. L. Zhang, *Phys. Plasmas* **20**, 012510 (2013).
- <sup>37</sup>H. Zhang, Z. Qiu, L. Chen, and Z. Lin, *Nucl. Fusion* **49**, 125009 (2009).
- <sup>38</sup>H. Zhang and Z. Lin, *Phys. Plasmas* **17**, 072502 (2010).
- <sup>39</sup>S. Briguglio, G. Vlad, F. Zonca, and C. Kar, *Phys. Plasmas* **2**, 3711 (1995).
- <sup>40</sup>S. Briguglio, F. Zonca, and G. Vlad, *Phys. Plasmas* **5**, 3287 (1998).
- <sup>41</sup>S. Briguglio, G. Fogaccia, G. Vlad, F. Zonca, K. Shinohara *et al.*, *Phys. Plasmas* **14**, 055904 (2007).
- <sup>42</sup>G. Vlad, S. Briguglio, G. Fogaccia, F. Zonca *et al.*, *Nucl. Fusion* **49**, 075024 (2009).
- <sup>43</sup>I. Holod, W. Zhang, and Y. Xiao, *Phys. Plasmas* **16**, 122307 (2009).
- <sup>44</sup>A. J. Brizard and T. S. Hahm, *Rev. Mod. Phys.* **79**, 421 (2007).
- <sup>45</sup>W. Deng, Z. Lin, and I. Holod, *Nucl. Fusion* **52**, 023005 (2012).
- <sup>46</sup>G. Y. Fu and C. Z. Cheng, *Phys. Fluids B* **4**, 3722 (1992).